Efficiently photocatalytic conversion of amine to imidine via perylene diimides supramolecules with oxygen vacancy

Yingxin Guo [a], Bing Liu [a], Jiawei Zhang [a], Chuntao Wang [a], Guangli Wang [a], Chengsi Pan [a], Hui Zhao [a], Yuming Dong professor, Doctor [a],[*], Yongfa Zhu [b]

[a] International Joint Research Center for Photo-responsive Molecules and Materials, School of Chemical and Material Engineering, Jiangnan University, Wuxi 214122, China
[b] Department of Chemistry, Tsinghua University, Beijing 100084, China

A B S T R A C T

The utilization of photocatalytic oxidation technology for sustainable production of value-added chemicals has garnered significant attention. In the photocatalytic process, the transfer rate of photogenerated holes is considerably slower (2–3 orders of magnitude) than that of electrons. Consequently, the migration of photogenerated holes emerges as a critical bottleneck in achieving the efficient conversion of solar energy into value-added chemicals. To address these challenges, we synthesized a perylene diimides supramolecule with abundant oxygen vacancies (R-Ov-PDI) to enhance holes transfer processes. Photogenerated holes were selectively captured by negatively charged defect sites, triggering an attack on the C–N bond. Noticeably, the catalyst exhibited a remarkable benzylamine oxidation efficiency (31.3 mmol·g^{-1}·h^{-1}) under visible light, with a selectivity for imine surpassing 99%. Furthermore, it demonstrated excellent substrate generality, outperforming most reported all-organic photocatalysts by 1–2 orders of magnitude. This study prove a novel perspective for the systematic design of efficient organic photocatalysts.

1. Introduction

The photocatalytic synthesis of high-value chemicals has garnered significant attention because of its efficient energy conversion processes [1–3]. Among these, the selective oxidation coupling reaction from benzylamine to N-benzylidenebenzylamine (N-BA) has been of particular interest, due to the versatile applications of N-benzylidenebenzylamine in the synthesis of pharmaceutically and biologically active compounds [4–6]. It is necessary to undergo highly selective cleavage of NH$_2$-CH bonds during the oxidative coupling of benzylamine, but the C-N bonds in the benzylamine molecules have quite high bond energy (the average bond dissociation energy is 305 kJ·mol^{-1}). Which indicates that the photocatalytic cracking of the C-N bond becomes a rate-determining step [7]. Notably, the carbon atom in the C-N bond carries a negative charge, making it susceptible to attack by positively charged species in the catalytic system. Consequently, the presence of positively charged photogenerated holes (h$^+$) fundamentally influences the efficiency of photocatalytic benzylamine oxidation coupling [8,9]. As is well-known, the migration of photogenerated charge carriers through the bulk and surface of the photocatalyst to the reaction sites is crucial for initiating chemical reactions [10]. However, the attention paid to the photogenerated hole, including the holes transfer and the subsequent oxidation process, lags considerably behind the attention paid to the electron. In particular, the slow migration rate of holes (which is about two to three orders of magnitude slower than that of electrons [11]) and the sluggish dynamics of the oxidation reaction make holes prone to recombination with electrons. Therefore, the effective enrichment of holes become the rate-limiting step in the reaction [12], that is, maximizing hole utilization efficiency is of the most important significance for improving photocatalytic oxidation activity [13].

As a novel photocatalytic material, organic supramolecules exhibit advantages such as a broad spectral response, structural diversity, low cost, and environmental friendliness, presenting vast research and application prospects in the field of photocatalysis [14–16]. However, existing studies mostly focused on the optimization of monomer molecular structures, assembly modes, and charge carrier dynamics [17–20]. It is still not ideal to improve the utilization rate of

---

photogenerated holes in organic supramolecule. As a result, there is an urgent need to explore suitable strategies to strengthen the utilization of photogenerated holes in organic supramolecules, in order to achieve highly efficient C-N cleavage. Up to now, revealing the holes transfer process and designing photocatalysts with efficient holes transfer remain significant challenges [21,22].

In this study, β-alanine-functionalized perylene diimides supramolecules was selected as a model photocatalyst and innovatively prepared perylene diimides supramolecules with oxygen vacancies (R-Ov-PDI). The oxygen vacancies in perylene diimides supramolecules, on the one hand, serves as trapping sites for photogenerated holes, and makes more positive photogenerated holes enter the antibonding π orbitals of adsorbed C-N, decreasing the potential barrier of the C-N bond in benzylamine oxidation. This markedly promotes the selectivity and activity of N-BA generation. On the other hand, owing to the efficient utilization of photogenerated holes, the concentration of photoelectrons involved in oxygen reduction increases, leading to the generation of abundant reactive oxygen species. The photogenerated holes and superoxide radicals synergistically accelerated the oxidation kinetics. With these advantages, R-Ov-PDI catalyzed the oxidative coupling reaction efficiently and stably, achieving a significant breakthrough in both material and performance. Compared to perylene diimides supramolecules without vacancies, the performance of R-Ov-PDI is markedly improved by 8.3 times. To our knowledge, this represents a 1–2 order of magnitude improvement over most existing all-organic photocatalysts in the photocatalytic BA oxidation coupling system.

2. Experimental section

2.1. Preparation of photocatalysts

0.3 mmol Bi(NO$_3$)$_3$·5H$_2$O and 25 mg PVP were added to a 50 mL ethylene glycol aqueous solution and stirred for 1 h. Subsequently, 5 mL DMF and 0.45 mmol SA-PDI were added. Perylene diimide (PDI) was synthesized by following previous work, please refer to Support information for more details.The resulting mixture was sealed in a 100 mL Teflon-linedstainless autoclave and heated at 190℃ for 4 h, followed by cooling to room temperature. The reaction product was washed with 50 mL 4 M HCl and 50 mL 2 M HNO$_3$, respectively. The obtained sample was washed with distilled water and ethanol, dried under vacuum at 60 ℃, and labeled as R-Ov-PDI. As a comparison, low-oxygen vacancy PDI nanosheets (P-Ov-PDI) were synthesized under the same reaction conditions without adding Bi (NO$_3$)$_3$·5H$_2$O. The synthesis route is shown in Scheme S1.

2.2. Sample characterization

Chemical structure was determined by the solid-state ^{13}C cross polarization magic angle spinning (^{13}C-CP/MAS) NMR spectrometer (AVANCE III HD 400, Bruker., Germany). Powder X-ray diffraction (D8, Bruker, Germany) was used for characterization. Transmission infrared and in-situ diffuse reflectance infrared spectra were recorded through the Fourier transform-infrared (FT-IR) spectrometer (Nicolet 6700, Thermo Fisher Scientific, United States). In-situ infrared spectra were measured using an infrared spectrometer (Nicolet iS50, Thermo Scientific, USA) with an MCT detector. Thermal stability was evaluated via the simultaneous thermal analyzer (TGA2 SF/1100, METTLER TOLEDO, Switzerland) in N$_2$ atmosphere at a heating rate of 10 °C min^{-1}.UV–vis diffuse reflectance spectra were obtained from the spectrometer (UV-3600 plus, Shimadzu, Japan) furnished with an integrating sphere device. The morphology and structure of the materials were characterized via field-emission scanning electron microscopy (S4800, Hitachi, Japan) and transmission electron microscopy (2100 plus, JEOL, Japan). To detect surface species of sample, X-ray photoelectron spectroscopy (XPS) analysis was conducted using an ESCALAB 250 Xi (Thermofisher, America) X-ray photoelectron spectrometer with Al Kα line as the

excitation source (hν =1484.8 eV) and adventitious carbon (284.8 eV for binding energy) was used as reference to correct the binding energy of sample. And surface photovoltage (SPV) was measured by homemade equipment.Using a fluorescence spectrometer with an excitation wavelength of 480 nm and ultrafast time-resolved fluorescence spectrometer (TRFLS, Lifespec II) to measure the characteristics of photogenerated carriers. The Kelvin probe force microscopy (KPFM) was carried out by SPM-9700HT (Shimadzu, Japan). Electron spin resonance (ESR) signals of spin-trapped paramagnetic species with 5, 5-dimethyl-1-pyrroline-N-oxide (DMPO) were detected using a Bruker A300E spectrometer (Bruker AXS Co., Germany). The electrochemical workstation (CHI660D, Shanghai Chenhua Instrument Co., Ltd.) was used to measure the EIS Nyquist spectra, cyclic voltammetry (CV), and Mott-Schottky curves of the photocatalyst, and transient photocurrent was measured under 300 W xenon lamp conditions.

2.3. Photocatalytic activity tests

Oxidation experiment for aerobic couplings of BA :
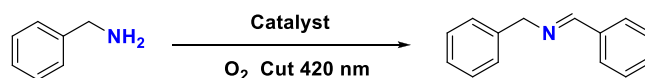
In a typical run, 1 mmol BA and 10 mL CH$_3$CN were charged into a 25 mL quartz flask with a magnetic stirring at the speed of 800 rpm. The R-Ov-PDI catalyst (8 mg) was then dispersed into the reactant solution, oxygen was passed for 30 min, and then the reaction was carried out under a 300 W Xe lamp (PLS-SXE300E, Beijing Perfectlight Technology Co., Ltd.) equipped with a 420 nm-cutoff filter. After the reaction, the supernatant was collected by centrifugation and analyzed using Nexis GC-2030, Shimadzu, Japan.

In order to further understand the photocatalytic mechanism of R-Ov-PDI, different sacrificial agents were used for trapping experiments, such as Mn(OAc)$_2$ as electron scavenger, benzoquinone(BQ) as ·O$_2^-$ scavenger, KI as hole scavenger and isopropanol (IPA) as ·OH scavenger.

The conversion of BA and the selectivity of N-BA were determined using the internal standard method using mesitylene as the internal standard. The conversion of other benzylamines and the selectivity of the corresponding imines were determined by area normalization.

The selectivity and conversion of BA to N-BA were calculated according to the following formula [3]:

$$Conversion \quad (\%) = 100 \times \frac{C_0 - C_{benzylamine}}{C_0}$$

$$Selectivity \quad (\%) = 100 \times \frac{2C_{N-benzylidenebenzylamine}}{C_0 - C_{benzylamine}}$$

$$TOF = \frac{moles_{benzylamine}(mmol) * Conversion_{benzylamine}}{m_{cat.}(g) * Time(s)}$$

Where C_0 is the initial amount of benzylamine, $C_{benzylamine}$ and $C_{N-benzylidenebenzylamine}$ are the amounts of the substrate benzylamine and its corresponding product of N-benzylidenebenzylamine, respectively.

The calibration curve is shown in supporting information, and a good linear relation (R^2 = 0.999) is observed between peak area and concentration.

2.4. H$_2$O$_2$ determination

The content of H$_2$O$_2$ was detected by the potassium titanium oxalate method [4]. Briefly, 3 mL of the sample solution was collected into a plastic centrifuge tube (10 mL), followed by the addition of 2 mL of potassium titanium oxalate solution (0.5 M). After shaking and stabilizing for min, the absorbance of the mixed solution was measured at a wavelength of 400 nm. The calibration curve is shown in supporting

information, and a good linear relation ($R^2 = 0.9999$) is observed between peak area and concentration.

2.5. Calculation details

All the spin-polarized density functional theory (DFT) calculations were performed by using the Vienna ab initio simulation package (VASP) [5,6]. The D3 correction method (DFT-D3) was employed in order to include van der Waals (vdW) interactions [7]. The projector-augmented wave (PAW) method was used to represent core-valence interactions [8]. Valence electrons were described by a plane wave basis with an energy cutoff of 400 eV. The generalized gradient approximation with the Perdew-Burke-Ernzerhof (GGA-PBE) functional was used to model electronic exchange and correlation [9]. Electron smearing was employed via Gaussian smearing method with a smearing width consistent to 0.05 eV. The conjugate gradient algorithm was used in geometry optimization calculations. Optimized structures were obtained by minimizing the forces on each ion until they were less than 0.03 eV/Å. The energy convergence criteria was set to 10^{-5} eV. The Brillouin zone was sampled at the $3\times3\times1$ k-point mesh. The adsorption energy (Eads) is defined as follows.

$$E_{ads} = E_{adsorbate/substrate} - E_{adsorbate} - E_{substrate}$$

Where $E_{adsorbate/surface}$, $E_{adsorbate}$ and $E_{substrate}$ represent the energies of substrate with the adsorbate species, the adsorbate molecule, and the substrate, respectively. A negative value means the process is exothermic adsorption.

3. Results and discussion

3.1. Structural characterization of perylene imide supermolecules with oxygen defects

The exceptional chemical tunability of perylene diimides (PDI) supramolecules offers a great opportunity to optimize the molecular structure of PDI by defect engineering. At the same time, because Bi^{3+} has a large ion radius (1.17 Å) and unique deformability, it can provide empty orbits for external electrons and overcome the steric resistance to form a complex. The synthesis method, as illustrated in Fig. 1a, in a hydrothermal reactor, carboxylic acid-functionalized perylene diimides supramolecules coordinate with Bi^{3+} to form the -COO-Bi- coordinated precursor. Following solvent-thermal processing, the two-step acid treatments resulted in the coordination precursor hydrolyzed. The process led to oxygen atom was removed from the lattice, creating oxygen vacancies. Under strong acid conditions, hydroxyl groups self-assembled to form perylene diimides supramolecules rich in oxygen vacancies (R-Ov-PDI). Thermal gravimetric analysis results (Fig. S1) indicated that the thermal loss temperature of R-Ov-PDI far exceeded the preparation temperature (190 °C). This confirmed that our synthetic method hardly disrupt the overall structure of the perylene core in PDI monomers. Morphological characterization of PDI and R-Ov-PDI was conducted using transmission electron microscopy (TEM).
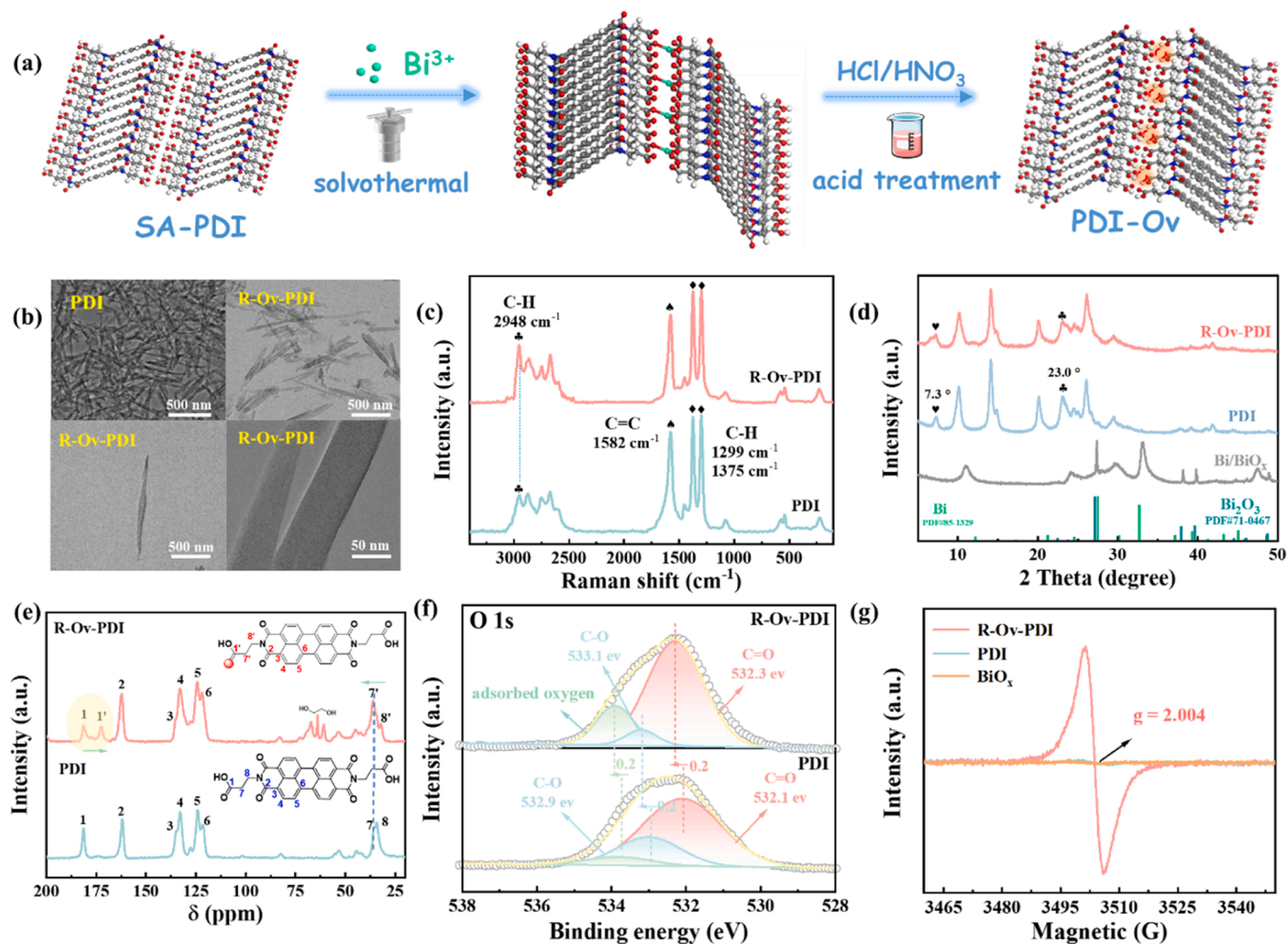

Fig. 1. (a).Schematic illustration of the synthetic process for R-Ov-PDI, (b) TEM images, (c) Raman spectra, and (d) XRD patterns of PDI and R-Ov-PDI, (e) Solid-state ^{13}C NMR spectra of PDI and R-Ov-PDI, (f) High-resolution XPS spectra of O1s in the R-Ov-PDI sample, (g) EPR spectra of different synthesized catalysts.

R-Ov-PDI exhibits a fibrous structure that is the typical morphology of Perylene diimides supramolecules [23,24]. It is confirmed the absence of bismuth oxide or elemental bismuth on the material surface due to the introduction of Bi^{3+} (Fig. 1b). Fourier transform infrared spectroscopy (FTIR, Figure S2) shows a weakening in the characteristic band at 936 cm^{-1}, which is attributed to the -OH groups connected to the C═O[25–27], indicating a change in the C═O of the carboxyl group in R-Ov-PDI and thus affecting the hydrogen bonding of the hydroxyl group.

Similarly, as revealed in Fig. 1c, R-Ov-PDI's Raman spectrum indicates a significantly enhanced peak at 2948 cm^{-1}, assigned to β-C-H, confirming a change in the molecular symmetry of R-Ov-PDI. Powder X-ray diffraction (XRD) demonstrates that the diffraction peaks of R-Ov-PDI align well with the corresponding PDI XRD spectrum. Due to the π-π stacking assembly, R-Ov-PDI also maintains good crystallinity (Fig. 1d). Notably, the signal peaks at 7.3° and 23.0° for the R-Ov-PDI gradually become broader and weaker, indicating that the defects alters the molecular structure of PDI, forming oxygen vacancies. The ^{13}C NMR spectrum shows a new signal for R-Ov-PDI at 172 ppm, distinct from PDI, attributed to the C atom adjacent to the O-defect in the carboxyl group. This signal exhibits a trend toward higher fields (Fig. 1e), expressing an increase in electron cloud density around the adjacent C atom due to the departure of the strongly electronegative oxygen atoms. As the electron cloud density around C atoms is a major factor influencing chemical shift (δ_C), the loss of O atoms results in a decrease in local electron cloud density, weakening the shielding effect, causing the δ_C of C atoms around O-defect sites to shift to low-field. X-ray photoelectron spectroscopy (XPS) confirms the surface electronic structure of R-Ov-PDI, and as expected, the elemental composition of R-Ov-PDI aligns closely with PDI (Fig. S3). The O 1 s XPS spectra of R-Ov-PDI and PDI exhibit triplet peaks. Similar to PDI, peaks centered at 532.1–532.3 and 532.9–533.1 eV are attributed to C═O and C-O in R-Ov-PDI, respectively. The peak centered at 533.9 eV is attributed to the oxygen atoms surrounding oxygen vacancies [28]. In comparison with PDI, both the binding energies of C═O and C–O in R-Ov-PDI exhibit a noticeable blue shift of 0.2 eV, corresponding to an increased of electron delocalization due to oxygen vacancies in the supramolecule (Fig. 1f)[29]. Additionally, all C and N peaks of R-Ov-PDI shift to lower energies by approximately 0.2 eV compared to the peaks of PDI (Fig. S4-5). This shift is attributed to the increased electron density around C and N atoms due to the absence of neighboring oxygen atoms, which is undoubtedly conducive to promoting the adsorption of substrate molecules and enhancing photocatalytic performance [30]. Electron paramagnetic resonance (EPR) spectroscopy is a magnetic resonance technique originating from the unpaired electron magnetic moment outside the nucleus, which can be employed to detect unpaired electrons in oxygen vacancies in substances. As shown in Fig. 1g, R-Ov-PDI exhibits a strong symmetrical resonance signal centered at g = 2.004, directly confirming the successful preparation of oxygen vacancies. Although the introduction of Bi is inevitable during material preparation, no unpaired electrons associated with oxygen vacancies were detected in the synthesized BiOx under the same preparation conditions. This suggests that the formation of oxygen vacancies primarily result from the perylene imide supermolecule. Elemental analysis (EA) further confirms the loss of some oxygen atoms (Table S1), with the O atom content in R-Ov-PDI being 19.92%, Markedly lower than that in PDI (22.40%). Correspondingly, density functional theory calculations further support the expected structure of R-Ov-PDI (Fig. S8). The optical absorption properties of the samples are characterized by UV-Vis diffuse reflectance spectroscopy (DRS). The intrinsic absorption of PDI occurs at 745 nm, while a red-shifted absorption edge (754 nm) is observed in R-Ov-PDI, indicating that oxygen vacancies extend the visible light absorption range of PDI, beneficial for improving its photocatalytic performance (Fig. S7). Furthermore, the presence of oxygen vacancies lowers the conduction band position of the material (from −0.42 eV to −0.40 eV), narrowing the bandgap (from 1.74 eV to 1.70 eV) (Fig. S8-10), and

promotes the transport of photogenerated charge carriers, facilitating photocatalytic kinetics to a certain extent. Corresponding density functional theory calculations provide robust theoretical support for this conclusion.

3.2. Excellent photocatalytic performance of perylene imide supermolecules with oxygen vacancy

As illustrated in Fig. 2a and Fig. S13, R-Ov-PDI demonstrates outstanding photocatalytic performance in the visible light-driven selective oxidation of benzylamine (BA). Under about 4 h of visible light irradiation, R-Ov-PDI attains nearly complete photo-oxidation of BA, resulting in the formation of N-BA with an almost 100% selectivity. The extraordinary BA oxidation rate up to 31.3 mmol·g^{-1}·h^{-1}, representing a substantial improvement compared to original PDI (with a BA conversion rate of 12%). The N-BA yield at the conclusion of the reaction experiences an approximately 13-fold enhancement. With an extended duration of irradiation, as presented in Fig. 2b, the photocatalytic oxidation of BA by R-Ov-PDI adheres to pseudo-first-order kinetics. The rate constant k_1 is around 35 times than k_2, where k_1 and k_2 correspond to the oxidation of BA to N-BA facilitated by R-Ov-PDI and pure PDI, respectively. In the reaction process, we also detected the oxidative dehydrogenation byproduct H_2O_2. The H_2O_2 generated by R-Ov-PDI efficiently oxidizing BA to N-BA was significantly higher than that generated by PDI (~8 times), which is consistent with the activity data (Fig. 2c). Through systematic comparison, the photocatalytic performance of R-Ov-PDI in this work is fairly better than most known photocatalytic BA oxidation systems (Fig. 2d; TableS2), including some noble metal-based photocatalysts. In addition, Fig. 2e shows that R-Ov-PDI still exhibits good catalytic activity after 4 cycles of selective oxidation of BA under light irradiation. The electron structure of R-Ov-PDI is characterized by EPR, the results show that it remains unchanged after the multiple cycling experiment (Fig. 2f). And no significant change is observable in either the PXRD pattern,SEM image,and XPS spectra after the reaction (Figure S14-15).We further obtained the reaction activity-molecular structure correlation of R-Ov-PDI during the oxidation process through a series of substrate expansion experiments (Table 1). In all cases, the conversion efficiency was above 90%, and the selectivity was nearly 100%, comparable or better than BA. In particular, compared with BA oxidation, when the benzene ring is substituted with an electron-withdrawing group, the substrate conversion can be further improved, while it decreases when the benzene ring is substituted with an electron-donating group. This implies that electron-withdrawing groups are more favorable for the progress of this reaction.

3.3. Photogenerated holes act as main reactive species trapped by oxygen defects in perylene imide supermolecules

Following this, we analyzed the Hammett plot of R-Ov-PDI for the photocatalytic selective oxidation of various para-substituted benzylamines. As depicted in Fig. 3a and Fig. S16, with a Hammett constant (ρ) of 0.3846, it indicates that during the photooxidation of benzylamine to N-BA on R-Ov-PDI, electron-withdrawing substituents promote the reaction, suggesting an accumulation of negative charge from reactants to transition states [31]. This finding is further substantiated by Table S3, where carbon atoms in the benzylamine molecule are negatively charged, revealing an affinity to associate with positively charged active sites in the catalyst. Therefore, the efficient utilization of abundant photogenerated holes becomes imperative to expedite the photooxidation activation of benzylamine.

We selectively captured ·OH, photogenerated holes, photogenerated electrons, and ·O_2^- in the reaction system, by employing IPA, KI, Mn (OAc)$_2$, and p-benzoquinone [17], respectively, for the purpose of gauging the influence of photogenerated holes on the catalytic oxidation of benzylamine. The results also indicate that electrons, ·O_2^- and holes are the major active species in the photooxidation of amines catalyzed
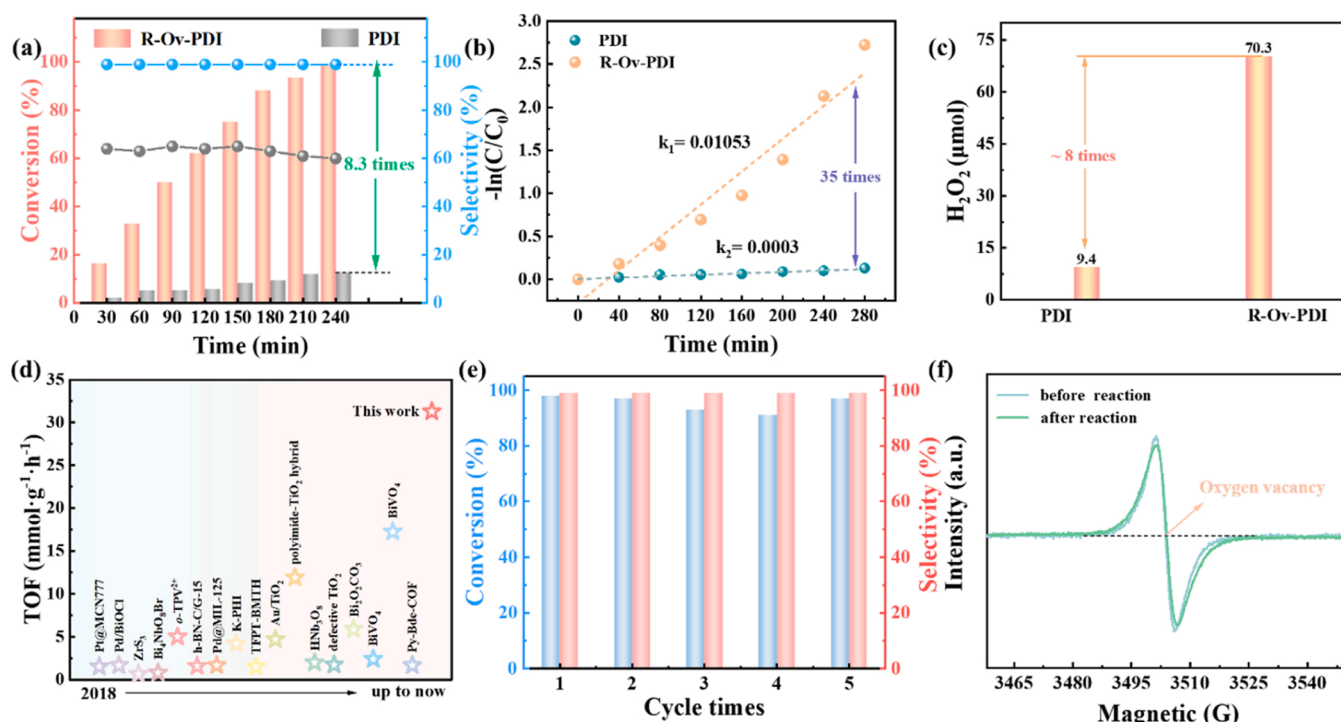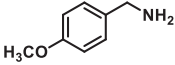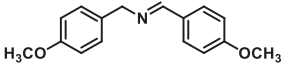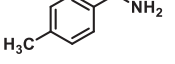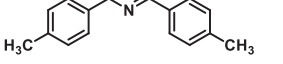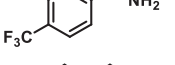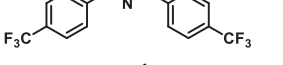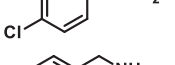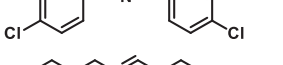
Fig. 2. (a) Comparison of photocatalytic oxidation of BA in O_2 on different samples (reaction time 4 h), (b) First order kinetic curve of different samples, (c)Evolution of H_2O_2 by the respective photocatalysts under visible light irradiation, (d) Comparison of herein reported benzylamine oxidation results with other photocatalysts over recent years, (e) Stability test for R-Ov-PDI sample; (f) EPR spectra for as-synthesized R-Ov-PDI and R-Ov-PDI sample after photocatalytic reaction.
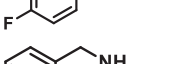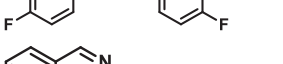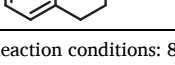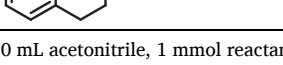
Table 1
Photocatalytic oxidation of benzylamine with different functional groups substituted on R-Ov-PDI.

Substrate	Product	Selectivity (%)	Conversion (%)	reaction time (h)
H_3CO—benzyl—NH_2	H_3CO—benzyl—N=benzyl—OCH_3	>99.9	>90	8
H_3C—benzyl—NH_2	H_3C—benzyl—N=benzyl—CH_3	>99.9	>90	10
F_3C—benzyl—NH_2	F_3C—benzyl—N=benzyl—CF_3	>99.9	>90	3
Cl—benzyl—NH_2	Cl—benzyl—N=benzyl—Cl	>99.9	>90	4
F—benzyl—NH_2	F—benzyl—N=benzyl—F	>99.9	>90	4
tetrahydroisoquinoline—NH	dihydroisoquinoline—N	>99.9	>90	6

Reaction conditions: 8 mg catalyst, 10 mL acetonitrile, 1 mmol reactant, illuminate 4 h under Xenon lamp (λ > 420 nm)

by R-Ov-PDI (Fig. 3b). Subsequently, we examined the benzylamine oxidation coupling process via cyclic voltammetry (Fig. 3c). The first oxidation peak current gradually increased with the addition of benzylamine, representing the crucial role of photo generated holes in benzylamine oxidation [32]. Oxygen vacancies play multiple roles in the process of photogenerated holes enrichment: firstly, the defects capture photogenerated holes, promoting the activation and dissociation of benzylamine molecules; secondly, they can facilitate the separation of photogenerated charges, inhibiting the recombination of holes and electrons. Therefore, understanding the role of c in the process of capturing photogenerated holes is of great significance for improving the efficiency of solar energy photocatalytic conversion. According to

the Kanada model, the efficiency of photogenerated hole-electron separation is positively correlated with the Zeta potential [33]. As presented in Fig. 3d, the Zeta potential $\zeta_{R-Ov-PDI}$ is −28.4 mV, significantly higher than ζ_{PDI} =-9.5 mV, implying that the oxygen vacancies increase the electron density of the material [34], providing a prerequisite for the enrichment of photogenerated holes. Obviously, the surface potential of R-Ov-PDI (ΔE = 84.3 mV) is much higher than that of PDI (ΔE = 23.6 mV) (Fig. 3e). As expected, the surface defects of R-Ov-PDI can act as capture centers for photogenerated charge carriers, transferring captured photogenerated holes and electrons to the adsorbed molecules, effectively preventing carrier recombination [35]. In situ X-ray photoelectron spectroscopy (in situ-XPS) in Fig. 3f reveals changes in binding
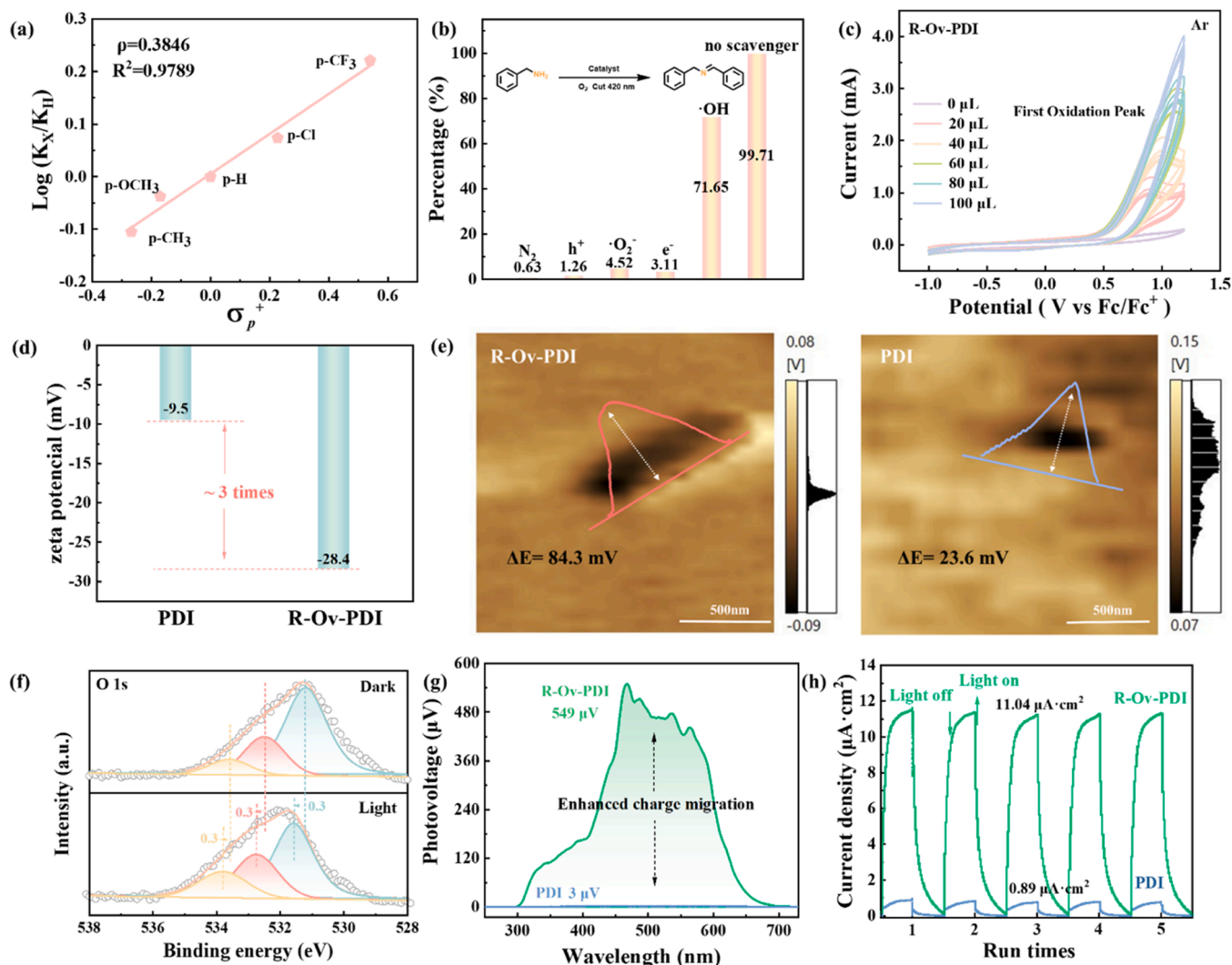
Fig. 3. (a) Hammett plot for the photocatalytic oxidation of para-substituted benzylamines over R-Ov-PDI, (b) The species trapping experiments for oxidation of BA to N-BA, (c) Cyclic voltammetry tests for R-Ov-PDI at different benzylamine concentrations in CH$_3$CN. (d) Zeta potential of PDI and R-Ov-PDI, (e) Surface potential of R-Ov PDI and PDI detected with KPFM, (f) O 1 s XPS spectra for R-Ov-PDI sample under dark and light irradiation, (g) Surface photovoltage and (h) Transient photocurrent response of synthesized photocatalysts.

energy under light conditions for various elements. Under light exposure, the O 1 s peak of R-Ov-PDI moves approximately 0.3 eV towards higher binding energy. This is because the enrichment of photogenerated holes on oxygen vacancies reduces the outer electron density of neighboring oxygen atoms. While the C 1 s and N 1 s peaks move towards lower binding energy, confirming that photogenerated holes in the catalyst flow towards oxygen vacancies under irradiation. Surface photovoltage (SPV) can not only reflect the separation efficiency of photogenerated charge carriers in materials, but also effectively provide the microscopic dynamic information of photogenerated charge carriers separation and charge transport capability in materials. As exhibited in Fig. 3g, R-Ov-PDI exhibits a positive surface photovoltage signal in the range of 300–700 nm, indicating that after light excitation, photogenerated holes of R-Ov-PDI act as the primary charge carriers transferred to the catalyst surface [36]. Meanwhile, compared to PDI, the surface photovoltage response is enormously enhanced (183 times), implying that more charge carriers migrate to the surface. To further illustrate the effective enrichment of photogenerated holes, we measured the photocurrent and in situ electrochemical impedance spectroscopy (EIS) of the synthesized photocatalyst. Compared to PDI, the photocurrent density of R-Ov-PDI (11.04 μA·cm^{-2}) has a 12-fold increase with light on/off cycles (PDI's photocurrent density is only

0.89 μA·cm^{-2}) (Fig. 3h). This suggests the effective enrichment of photogenerated holes is beneficial to the transfer of photogenerated charge carriers [36]. The Nyquist plot radius of R-Ov-PDI in the EIS spectrum is significantly smaller than that of PDI & P-Ov-PDI, suggesting lower charge transfer resistance in the R-Ov-PDI system, ensuring faster holes transfer [37]. Under visible light irradiation, the radius of the Nyquist curve decreases, meaning the effective transfer process of photogenerated holes (Fig. S17). The PL spectra of PDI and R-Ov-PDI are shown in Fig. S18. Compared to PDI (PDI exhibits a strong and sharp emission peak at 718 nm), the emission of R-Ov-PDI shows significant quenching, illustrating effective inhibition of charge recombination due to the capture of photogenerated holes by oxygen vacancies [38]. Furthermore, affected by the oxygen vacancies on the charge distribution inside the molecule, the emission peak of R-Ov-PDI undergoes a significant blue shift towards 702 nm [39]. This conclusion is supported again by time-resolved fluorescence spectroscopy fitting dynamics decay curves (Fig. S19). All the aforementioned data demonstrate that R-Ov-PDI exhibits better capability for the separation of photogenerated charge carriers under light conditions.

In Fig. 4a, the characteristic peak of imine on R-Ov-PDI at 1113–1433 cm^{-1} exhibits a particularly evident signal shortly after the light is turned on, contrasting sharply with the weak indication observed
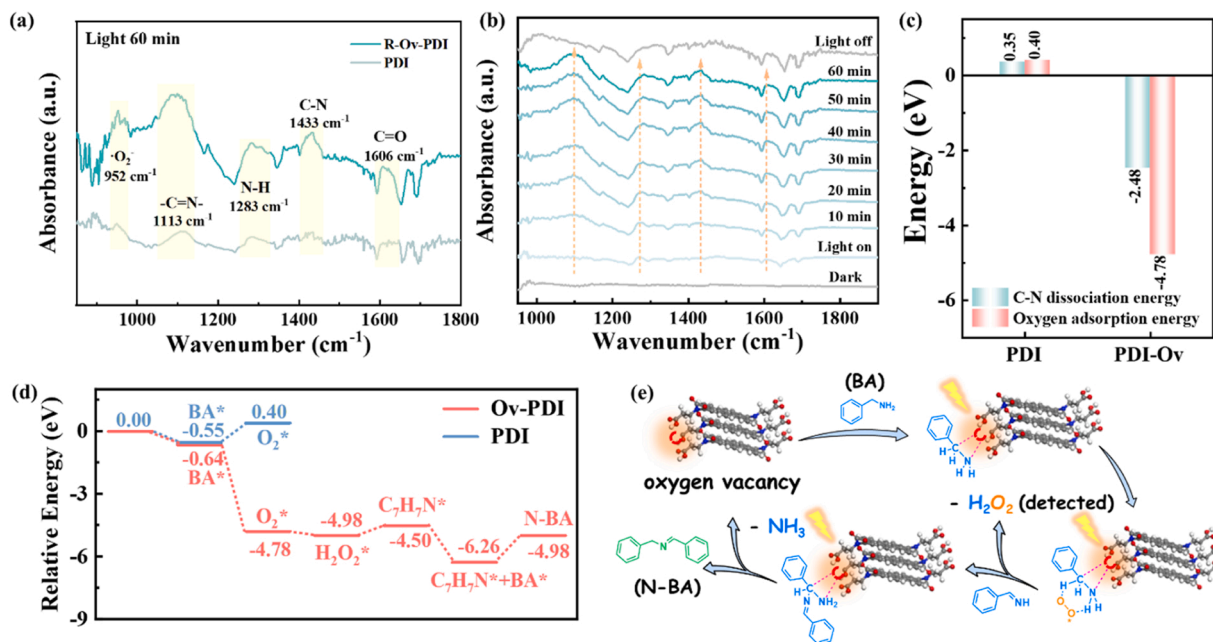
Fig. 4. (a) In situ FT-IR spectra of PDI and R-Ov-PDI after 60 min of illumination, (b) In situ FT-IR spectra vs illumination time for the photocatalytic system of R-Ov-PDI, (c) Adsorption energy of O_2 on R-Ov-PDI adsorbed benzylamine and dissociation energy of C-N on R-Ov-PDI, (d) Calculated free energy diagrams of oxygen reduction and benzylamine oxidation pathways on different photocatalysts. (e) Tentative Mechanism of the Photocatalysis Oxidation Process with R-Ov-PDI.

at the same wavenumber on PDI. Besides, owing to a more utilization of photogenerated holes, the $\cdot O_2^-$ signal at 952 cm^{-1} on R-Ov-PDI reflects significantly stronger oxygen reduction reaction (ORR) performance compared to PDI. To demonstrate the favorable role of O vacancies in O_2 reduction, $\cdot O_2^-$ concentration were monitored with 3,3′, 5, 5′ tetramethylbenzidine (TMB) as an indicator molecule by monitoring the absorbance change in the solution at different time intervals. The time-dependent absorption spectra of TMB oxidation (Figure S20) displayed the enhanced concentration of generated superoxide radicals for R-Ov-PDI. Furthermore, ESR test was used to further verify the role of $\cdot O_2^-$ in photocatalytic H_2O_2 generation progress. As shown in Figure S21, the pronounced EPR signal on R-Ov-PDI and strongly supports this conclusion. As the reaction progresses, the $\cdot O_2^-$ is continuously consumed, and the signal intensity decreases with the extended illumination time in the photocatalytic system [40] (Fig. S22). Particularly, the signal strength at the imine characteristic position extremely enhances with the prolonged illumination time, directly confirming the pivotal role of R-Ov-PDI in process of C-N cleavage (Fig. 4b). As shown in Fig. 4c and Fig. S23, theoretical calculations also confirm that the introduction of oxygen vacancies reduce the energy barrier of the rate-determining step for C-N dissociation from 0.35 eV to −2.48 eV. In addition, the O_2-TPD results also confirmed the favourable oxygen adsorption effect of vacancies (Fig. S24). This is attributed to the oxygen vacancies adjusting the electronic state of the active site. Moreover, the introduction of oxygen vacancies facilitates the adsorption of molecular oxygen by lowering the adsorption energy barrier from 0.40 eV to −4.78 eV due to efficient photogenerated holes utilization. To elucidate the reaction mechanism, we applied DFT calculations to explore the formation pathway of N-BA on the defect state of R-Ov-PDI. The ease of a reaction can be determined by the change in Gibbs free energy, the more negative it is, the easier the reaction will proceed. As shown in Fig. 4d, the Gibbs free energy change (ΔG) on the oxygen vacancies of R-Ov-PDI exhibits the most favorable conditions for the formation of intermediate species BA* and O–O*, suggesting that the enriched photogenerated holes localized in oxygen vacancies play a crucial role in the C–N bond cleavage process. The theoretical calculation results align with the in-situ infrared results. Compared to the original infrared spectrum of benzylamine molecules (Fig. S25), a distinct σ (N-H) bending vibration signal induced by

adsorbed benzylamine is observed under dark conditions in argon (Fig. S26). This demonstrates that, under dark conditions, benzylamine molecules adsorbed on the surface of R-Ov-PDI through charge interactions but did not receive further dissociation. In comparison with the peaks assigned to R-Ov-PDI, the XPS of R-Ov-PDI after dark adsorption of benzylamine shows a new peak attributed to C–NH$_2$, indicating a strong interaction between surface charges and benzylamine molecules [41] (Fig. 4b and S27–29).

The abruption of C-N and the coupling of C=N is a multi-step proton-coupled electron transfer (PCET) process, and several intermediates (N–H and N≡H) might appear in the DRIFTS spectrum. As expected, upon introducing O_2 into the in-situ reaction cell and initiating illumination, the signal of the N-H stretching vibration of benzylamine molecules gradually weakens with increasing illumination time, while the signal intensity of the C≡N bond gradually increases (Fig. S30). This confirms the continuous oxidation of benzylamine molecules during the reaction, producing highly reactive imine intermediates [42], making it easier for further coupling reactions with substrates to generate the target product. Especially, as shown in Fig. S31, upon continuously supplying oxygen and turning off the light source, the N-H signal belonging to the imine intermediate weakens with the prolonged dark period, and the signal of alkyl C–H gradually increases with time, indicating the dissociation of charge-transfer complex formed by NH-imine and benzylamine. It is confirmed that the pivotal role of photogenerated holes in the C-N bond cleavage on R-Ov-PDI photocatalyst. Meanwhile, we substantiated the reaction pathway through the detection of trace byproducts, benzonitrile (Fig. S32). Based on these observations, we propose the corresponding reaction mechanism. As illustrated in Fig. 4e, benzylamine is adsorbed on the carboxyl group through hydrogen bonding. At the same time, under light irradiation, superoxide radicals generated from the reduction of O_2 form electron complexes with C-H and N-H. Specifically, upon photoexcitation, oxygen vacancies, acting as charge traps, capture photogenerated holes carrying positive charges, effectively adsorbing the negatively charged C–N bond in benzylamine to form BA* [43]. Subsequently, the superoxide radicals (O–O*) form low-energy electron complexes with chemisorbed benzylamine molecules. After that, the generated H_2O_2 is desorbed from R-Ov-PDI, accompanied by the formation of the

intermediate NH-imine (C_7H_7*). Eventually, NH-imine and benzylamine form a low-energy electron adduct ($C_7H_7* + BA*$), which can easily undergo photogenerated holes-induced C-N cleavage, releasing NH_3 to generate the target product, thus imine (N-BA). Simultaneously, the active center is released, forming a catalytic cycle.

4. Conclusion

In summary, we employed a defect engineering strategy to enhance the photo-driven organic supramolecular catalysis for the conversion of amines to imines. Mechanistic studies reveal that oxygen vacancies serve as hole-trapping centers, enabling the effective accumulation of photogenerated holes to participate in photocatalytic oxidation reactions. Simultaneously, they stimulate the photogenerated electrons to reduce O_2, generating more superoxide radicals. The synergistic action of these processes accelerates the kinetics of C-N cleavage. Under the combined influence of these factors, R-Ov-PDI ultimately achieves an impressive BA oxidation efficiency of 31.3 $mmol \cdot g^{-1} \cdot h^{-1}$, surpassing the majority of reported organic photocatalysts. This study effectively modulates the utilization efficiency of photogenerated holes and systematically elucidates the promotion mechanism of oxygen vacancies in the C–N cleavage kinetics within organic semiconductors. It provides valuable insights for the design of high-performance organic photocatalysts.

CRediT authorship contribution statement

Jiawei Zhang: Methodology, Formal analysis. **Chuntao Wang:** Investigation. **Guangli Wang:** Supervision. **Chengsi Pan:** Supervision. **Yingxin Guo:** Writing – review & editing, Writing – original draft, Validation, Methodology, Investigation, Formal analysis, Conceptualization. **Bing Liu:** Methodology. **Yuming Dong:** Writing – review & editing, Writing – original draft, Supervision, Resources, Project administration, Investigation, Funding acquisition, Formal analysis. **Yongfa Zhu:** Supervision, Resources. **Hui Zhao:** Supervision.

Declaration of Competing Interest

The authors declare that they have no known competing financial interests or personal relationships that could have appeared to influence the work reported in this paper.

Data availability

Data will be made available on request.

Acknowledgements

Appendix A. Supporting information

Supplementary data associated with this article can be found in the online version at doi:10.1016/j.apcatb.2024.123915.

References

[1] W. Xie, K. Li, X.H. Liu, X. Zhang, H. Huang, P-mediated Cu-N_4 sites in carbon nitride realizing CO_2 photoreduction to C_2H_4 with selectivity modulation, Adv. Mater. 35 (2022) e2208132.

[2] X. Jie, S. Gonzalez-Cortes, T. Xiao, B. Yao, J. Wang, D.R. Slocombe, Y. Fang, N. Miller, H.A. Al-Megren, J.R. Dilworth, J.M. Thomas, P.P. Edwards, The decarbonisation of petroleum and other fossil hydrocarbon fuels for the facile production and safe storage of hydrogen, Energy Environ. Sci. 12 (2019) 238–249.

[3] M. Lv, F. Tong, Z. Wang, Y. Liu, P. Wang, H. Cheng, Y. Dai, Z. Zheng, B. Huang, $BiVO_4$ quadrangular nanoprisms with highly exposed {101} facets for selective photocatalytic oxidation of benzylamine, J. Mater. Chem. A 10 (2022) 19699–19709.

[4] W. Xu, B. Huang, G. Li, F. Yang, W. Lin, J. Gu, H. Deng, Z. Gu, H. Jin, Donor-acceptor mixed-naphthalene diimide-porphyrin MOF for boosting photocatalytic oxidative coupling of amines, ACS Catal. 13 (2023) 5723–5732.

[5] Y. Guo, B. Liu, J. Zhang, G. Wang, C. Pan, H. Zhao, C. Wang, F. Yu, Y. Dong, Y. Zhu, Perylene imide supermolecule promote oxygen to superoxide radical for ultrafast photo-oxidation of 5-hydroxymethylfurfural, Appl. Catal. B. Environ. 340 (2024) 123217.

[6] P. Konga, H. Tan, T. Lei, J. Wang, W. Yan, R. Wang, E. Waclawikc, Z. Zheng, Z. Li, Oxygen vacancies confined in conjugated polyimide for promoted visible-light photocatalytic oxidative coupling of amines, Appl. Catal. B Environ 272 (2020) 118964.

[7] W. Man, J. Xie, Y. Pan, W. Lam, H. Kwong, K. Ip, S. Yiu, K. Lau, T. Lau, C-N bond cleavage of anilines by a (salen) ruthenium (VI) nitrido complex, J. Am. Chem. Soc. 135 (2013) 5533–5536.

[8] J. Qin, B. Han, X. Lu, J. Nie, C. Xian, Z. Zhang, Biomass-derived single Zn atom catalysts: the multiple roles of single Zn atoms in the oxidative cleavage of C-N bonds, JACS Au 3 (2023) 801–812.

[9] Y. Cui, Y. Wang, W. Tian, Y. Bu, T. Li, X. Cui, T. Zhu, R. Li, B. Wu, Development of a versatile and efficient C-N lyase platform for asymmetric hydroamination via computational enzyme redesign, Nat. Catal. 4 (2021) 364–373.

[10] R. Chen, Z. Ren, Y. Liang, G. Zhang, T. Dittrich, R. Liu, Y. Liu, Y. Zhao, S. Pang, H. An, C. Ni, P. Zhou, K. Han, F. Fan, C. Li, Spatiotemporal imaging of charge transfer in photocatalyst particles, Nature 610 (2022) 296–301.

[11] X. Li, B. Liu, M. Wen, Y. Gao, H. Wu, M. Huang, Z. Li, B. Chen, C. Tung, L. Wu, Hole-accepting-ligand-modified CdSe QDs for dramatic enhancement of photocatalytic and photoelectrochemical hydrogen evolution by solar energy, Adv. Sci. 3 (2016) 1500282.

[12] C. Zhang, Z. Shao, X. Zhang, G. Liu, Y. Zhang, L. Wu, C. Liu, Y. Pan, F. Su, M. Gao, Y. Li, S. Yu, Design principles for maximizing hole utilization of semiconductor quantum wires toward efficient photocatalysis, Angew. Chem. Int. Ed. 62 (2023) e202305571.

[13] Y. Li, S. Yu, J. Xiang, F. Zhang, A. Jiang, Y. Duan, C. Tang, Y. Cao, H. Guo, Y. Zhou, Revealing the importance of hole transfer: boosting photocatalytic hydrogen evolution by delicate modulation of photogenerated holes, ACS Catal. 13 (2023) 8281–8292.

[14] Y. Wang, A. Vogel, M. Sachs, R.S. Sprick, L. Wilbraham, S.J.A. Moniz, R. Godin, M. A. Zwijnenburg, J.R. Durrant, A.I. Cooper, J. Tang, Current understanding and challenges of solar-driven hydrogen generation using polymeric photocatalysts, Nat. Energy 4 (2019) 746–760.

[15] Z. Song, L. Miao, L. Ruhlmann, Y. Lv, L. Li, L. Gan, M. Liu, Proton-conductive supramolecular hydrogen-bonded organic superstructures for high-performance zinc-organic batteries, Angew. Chem. Int. Ed. 62 (2023) e202219136.

[16] J. Yu, L. Huang, Q. Tang, S. Yu, Q. Qi, J. Zhang, D. Ma, Y. Lei, J. Su, Y. Song, J. Eloi, R.L. Harniman, U. Borucu, L. Zhang, M. Zhu, F. Tian, L. Du, D.L. Phillips, I. Manners, R. Ye, J. Tian, Artificial spherical chromatophore nanomicelles for selective CO_2 reduction in water, Nat. Catal. 6 (2023) 464–475.

[17] Y. Sheng, We Li, L. Xu, Y. Zhu, High photocatalytic oxygen evolution via strong built-in electric field induced by high crystallinity of perylene imide supramolecule, Adv. Mater. 34 (2022) 2102354.

[18] Z. Zhang, X. Chen, H. Zhang, W. Liu, W. Zhu, Y. Zhu, A highly crystalline perylene imide polymer with the robust built-in electric field for efficient photocatalytic water oxidation, Adv. Mater. 32 (2020) 1907746.

[19] D. Liu, J. Wang, X. Bai, R. Zong, Y. Zhu, Self-assembled PDINH supramolecular system for photocatalysis under visible light, Adv. Mater. 28 (2016) 7284–7290.

[20] J. Wang, D. Liu, Y. Zhu, S. Zhou, S. Guan, Supramolecular packing dominant photocatalytic oxidation and anticancer performance of PDI, Appl. Catal. B: Environ. 231 (2018) 251–261.

[21] T. Han, X. Cao, H. Chen, J. Ma, Y. Yu, Y. Li, W. Xu, K. Sun, A. Huang, Z. Chen, C. Chen, H. Zhang, B. Ye, Q. Peng, Y. Li, Photosynthesis of benzonitriles on BiOBr nanosheets promoted by vacancy associates, Angew. Chem. Int. Ed. 62 (2023) e2023133.

[22] X. Zhang, P. Ma, C. Wang, L. Gan, X. Chen, P. Zhang, Y. Wang, H. Li, L. Wang, X. Zhou, K. Zheng, Unraveling the dual defect sites in graphite carbon nitride for ultra-high photocatalytic H_2O_2 evolution, Energy Environ. Sci. 15 (2022) 830–842.

[23] J. Wang, W. Shi, D. Liu, Z. Zhang, Y. Zhu, D. Wang, Supramolecular organic nanofibers with highly efficient and stable visible light photooxidation performance, Appl. Catal. B Environ. 202 (2017) 289–297.

[24] K. Zhang, J. Wang, W. Jiang, W. Yao, H. Yang, Y. Zhu, Self-assembled perylene diimide based supramolecular heterojunction with Bi_2WO_6 for efficient visible-light-driven photocatalysis, Appl. Catal. B Environ. 232 (2018) 175–181.

[25] K.H. Becker, H.W. Schmidt, Para-linked aromatic poly (amic ethyl esters): precursors to rodlike aromatic polyimides. 1. Synthesis and imidization study, Macromolecules 25 (1992) 6784–6790.

[26] F.M. Houlihan, B.J. Bachman, C.W. Wilkins, Jr, C.A. Pryde, Synthesis and characterization of the tert-butyl ester of the oxydianiline/pyromellitic dianhydride polyamic acid, Macromolecules 22 (1989) 4477–4483.

[27] Z. Zhang, Y. Zhu, X. Chen, H. Zhang, J. Wang, A full-spectrum metal-free porphyrin supramolecular photocatalyst for dual functions of highly efficient hydrogen and oxygen evolution, Adv. Mater. 31 (2019) 1806626.

[28] J. Yang, H. Miao, W. Li, H. Li, Y. Zhu, Designed synthesis of p-Ag_2S/n-PDI self-assembly supramolecular heterojunction for enhanced full-spectrum photocatalytic activity, J. Mater. Chem. A 27 (2019) 6482–6490.

[29] J. Xiong, J. Di, J. Xia, W. Zhu, H. Li, Surface defect engineering in 2D nanomaterials for photocatalysis, Adv. Funct. Mater. 28 (2018) 1801983.

[30] H. Liu, C. Xu, D. Li, H.L. Jiang, Photocatalytic hydrogen production coupled with Selective benzylamine oxidation over MOF composites, Angew. Chem. Int. Ed. 57 (2018) 5379–5383.

[31] S. Lin, C.S. Diercks, Y.-B. Zhang, N. Kornienko, E.M. Nichols, Y. Zhao, A.R. Paris, D. Kim, P. Yang, O.M. Yaghi, C.J. Chang, Covalent organic frameworks comprising cobalt porphyrins for catalytic CO_2 reduction in water, Science 349 (2015) 1208–1213.

[32] J. Xu, W. Li, W. Liu, J. Jing, K. Zhang, L. Liu, Dr.J. Yang, E. Zhu, J. Li, Y. Zhu, Efficient Photocatalytic hydrogen and oxygen evolution by side-group engineered benzodiimidazole oligomers with strong built-in electric fields and short-range crystallinity, Angew. Chem. Int. Ed. 61 (2022) e202212243.

[33] Y. Cao, L. Guo, M. Dan, D.E. Doronkin, C. Han, Z. Rao, Y. Liu, J. Meng, Z. Huang, K. Zheng, P. Chen, F. Dong, Y. Zhou, Modulating electron density of vacancy site by single Au atom for effective CO_2 photoreduction, Nat. Commun. 12 (2021) 1675.

[34] J. Yang, J. Jing, W. Li, Y. Zhu, Electron donor-acceptor interface of TPPS/PDI boosting charge transfer for efficient photocatalytic hydrogen evolution, Adv. Sci. 17 (2022) 2201134.

[35] J. Jing, J. Li, Y. Su, Y. Zhu, Non-covalently linked donor-acceptor interaction enhancing photocatalytic hydrogen evolution from porphyrin assembly, Appl. Catal. B Environ. 324 (2023) 122284.

[36] W. Li, Z. We, K. Zhu, W. Wei, J. Yang, J. Jing, D.L. Phillips, Y. Zhu, Nitrogen-defect induced trap states steering electron-hole migration in graphite carbon nitride, App. Catal. B Environ 306 (2022) 121142.

[37] Z. Zhou, J. Liu, R. Long, L. Li, L. Guo, O.V. Prezhdo, Control of charge carriers trapping and relaxation in hematite by oxygen vacancy charge: Ab initio non-adiabatic molecular dynamics, J. Am. Chem. Soc. 139 (2017) 6707–6717.

[38] Z. Wei, W. Wang, W. Li, X. Bai, J. Zhao, E.C.M. Tse, D.L. Phillips, Y. Zhu, Steering electron-hole migration pathways using oxygen vacancies in tungsten oxides to enhance their photocatalytic oxygen evolution performance, Angew. Chem. Int. Ed. 60 (2021) 8236–8242.

[39] J. Xu, X. Huang, X. Cheng, M. Whangbo, S. Deng, Microscopic mechanism of the heat-induced blueshift in phosphors and a logarithmic energy dependence on the nearest dopant-vacancy distance, Angew. Chem. Int. Ed. 61 (2022) e202116404.

[40] Q. Zhi, W. Liu, R. Jiang, X. Zhan, Y. Jin, X. Chen, X. Yang, K. Wang, W. Cao, D. Qi, J. Jiang, Piperazine-linked metal phthalocyanine frameworks for highly efficient visible-light-driven H_2O_2 photosynthesis, J. Am. Chem. Soc. 144 (2022) 21328–21336.

[41] Z. Tian, C. Han, Y. Zhao, W. Dai, X. Lian, Y. Wang, Y. Zheng, Y. Shi, X. Pan, Z. Huang, H. Li, W. Chen, Efficient photocatalytic hydrogen peroxide generation coupled with selective benzylamine oxidation over defective ZrS_3 nanobelts, Nat. Commun. 12 (2021) 2039.

[42] W. Wang, Y. Wang, R. Yang, Q. Wen, Y. Liu, Z. Jiang, H. Li, T. Zhai, Vacancy-rich $Ni(OH)_2$ drives the electro-oxidation of amino C-N bonds to nitrile C≡N bonds, Angew. Chem. Int. Ed. 59 (2020) 16974–16981.

[43] X. Zu, Y. Zhao, X. Li, R. Chen, W. Shao, Z. Wang, J. Hu, J. Zhu, Y. Pan, Y. Sun, Y. Xie, Ultrastable and efficient visible-light-driven CO_2 reduction triggered by regenerative oxygen-vacancies in $Bi_2O_2CO_3$ nanosheets, Angew. Chem. Int. Ed. 60 (2021) 13840–13846.